Gold nanobipyramid@cuprous oxide jujube-like nanostructures for plasmon-enhanced photocatalytic performance

Yujie Ma, Xingzhong Zhu, Shusheng Xu, Guili He, Lu Yao, Nantao Hu, Yanjie Su, Jie Feng, Yafei Zhang, Zhi Yang*

Key Laboratory of Thin Film and Microfabrication (Ministry of Education), Department of Micro/Nano Electronics, School of Electronic Information and Electrical Engineering, Shanghai Jiao Tong University, Shanghai 200240, P.R. China

ABSTRACT

Nobel metal/semiconductor composites is a kind of alluring photocatalysts based on their broad light absorption and high photocatalytic efficiency. In this work, we reported a novel jujube-like gold nanobipyramid core/cuprous oxide shell (Au NBP@Cu$_2$O) composite photocatalyst, with adjustable aspect ratio of Au NBP core and thickness of Cu$_2$O shell. The Au NBP@Cu$_2$O products possess tunable light absorption from visible to near-infrared region and all of them exhibit excellent photocatalytic performances compared with pure Cu$_2$O. The optimal Au NBP@Cu$_2$O sample achieves nearly 100% degradation of methyl orange in 60 min compared with 2.45% for pure Cu$_2$O under illumination ($\lambda > 400$ nm), and 47.5% degradation of methyl orange in 60 min compared with 1.23% for pure Cu$_2$O under illumination ($\lambda > 700$ nm). The enhanced photocatalytic behaviors are attributed to the efficient charge separation driven by Schottky junction in Au NBP@Cu$_2$O, as well as the strong surface plasmon resonance effect from Au NBPs which not only extends the light response for Cu$_2$O but also enhances the photodegradation by generating hot electrons to inject into Cu$_2$O. Furthermore, it is worth mentioning that the Au NBP@Cu$_2$O composites exhibit significantly enhanced stability because the Au NBP core can draw holes from Cu$_2$O. This work may provide guidance to the fabrication of plasmon-enhanced photocatalysts based on Au NBPs and other semiconductors along with the exploration of wider applications for them in the future work.

1. Introduction

Photocatalysis technology has attracted much attention these years because it provides an environmental-friendly and sustainable approach to remove contaminants efficiently with the utilization of inexhaustible solar energy [1–4]. Photocatalysts based on semiconductor materials have been widely studied because of their good stability, easy formation, low cost, and certainly excellent photocatalytic activity [5–7]. At present, there are two popular semiconductors, TiO$_2$ and ZnO, that have been extensively used as photocatalysts in previous studies and commercial applications [8–12]. However, both TiO$_2$ and ZnO are wide band-gap semiconductors and can only utilize ultraviolet light which accounts for less than 5% of the total solar energy. To take full use of solar energy, researchers have tuned attention to cuprous oxide (Cu$_2$O), a common narrow band-gap (2.17 eV) semiconductor, which is responsive to the visible light and thus able to harvest 45% of the total solar energy [13–16]. Apart from this, Cu$_2$O shows other advantages, such as lower toxicity, better environmental acceptability, as well as

more available formation at a reasonable cost when compared with other semiconductors [13,16]. But pure Cu$_2$O photocatalysts suffer from relatively low photocatalytic efficiency due to its low hole mobility and utilization. It may achieve effectively photocatalytic efficiency if providing a driving force to accelerate carrier migration and a hole sink to trap and separate holes from electrons on it. Among those approaches which were adopted to achieve the above target, such as doping elements in Cu$_2$O [17,18], combining noble metals with Cu$_2$O [19–21], and incorporating Cu$_2$O with other semiconductors or carbon materials [22–25], combining Cu$_2$O with plasmonic noble metal nanoparticles (e.g. Au, Ag and Cu) is an effective approach to promote charge separation and interfacial charge-transfer, and therefore prolong the lifetime of carriers to participate in photocatalysis [26–28]. Moreover, introducing these noble metals in Cu$_2$O can further expand the light absorption for Cu$_2$O owing to the surface plasmon resonance (SPR) effect, which is also significant for the improvement of photocatalytic performance [29].

Among the plasmonic noble metal nanoparticles, Au nanostructures

have attracted more attention because of their excellent stability under harsh conditions and especially their tunable SPR band based on abundant morphologies, such as Au nanoparticles (NPs) [30,31], Au nanowires [32,33], Au nanocubes [34,35], Au nanorods (NRs) [36–38], and Au nanobipyramids (NBPs) [39,40]. Till now, Au nanostructures have been commonly used in the fabrication with Cu_2O in previous studies, except for the Au NRs and Au NBPs. Different from common Au nanostructures, Au NRs and Au NBPs are fascinating which have elongated structures with not only transversal plasmon resonance wavelengths (TPRWs) in 520–540 nm region just like Au NPs, but also longitudinal plasmon resonance wavelengths (LPRWs) which can be synthetically tunable over a wide spectral range from visible to near-infrared region by adjusting the aspect ratios [41,42]. Furthermore, compared with Au NRs, Au NBPs have much stronger plasmon resonance due to their sharper tips, narrower shape, uniform size distributions, and wider SPR absorption range from visible to near-infrared region [40,43]. Therefore, it would be worthy of expecting to develop Au NBPs/Cu_2O composites with enhanced photocatalytic activity under visible and even near-infrared light, which is never reported at present. Moreover, for most of the reported Au NBPs/Cu_2O composites, Au nanostructures are usually deposited on the Cu_2O matrix [44–46], whereas the encapsulation of Au nanostructures into Cu_2O shells to form core-shelled Au@Cu_2O composites is relatively fewer [29,41,47]. We focused on the core-shelled Au@Cu_2O composites because they can offers a 3D close interaction between Au core and Cu_2O shell which will allow more efficient transfer of hot electrons from Au to Cu_2O. Besides, the core-shelled Au@Cu_2O composites can better maintain Au morphologies from photocorrosion and suspension, avoid the aggregation of Au nanostructures and prevent the Au nanostructures exposed outside as photoactive sites to produce by-products [43].

Herein, we developed a jujube-like Au NBP core@Cu_2O shell nanostructure with a simple approach, through which the geometry of Au NBP@Cu_2O (i.e. size and shell thickness) could be controlled by changing the Au NBP amounts and aspect ratios of Au NBPs. Due to the introduction of Au NBPs, Au NBP@Cu_2O composites show strong SPR absorption, which is tunable from visible and near-infrared region. Significantly, all the Au NBP@Cu_2O samples exhibit remarkably enhanced photocatalytic performances than pure Cu_2O under both visible and near-infrared light. We discuss the photocatalysis mechanism in details and present that holes can migrate from the Cu_2O shell to the Au NBP core, therefore making separation of holes and electrons on Cu_2O and enhancing the photocatalytic efficiency and stability of Au NBP@Cu_2O composites. Besides, Au NBPs exhibit strong SPR effect, which can extend the light response for Cu_2O as well as generate abundant hot electrons to inject into Cu_2O to improve its photocatalytic activity. The photocatalysis mechanism here has some differences from those reported previously. Additionally, it is also estimated that the aspect ratio of Au NBPs and the jujube-like structure of Au NBP@Cu_2O may influence the photocatalytic performance. We hope our results will provide guided information for the development of Au NBPs and Cu_2O or other semiconductor composites to achieve plasmon-enhanced photocatalytic performance under visible and near-infrared light.

2. Experimental section

2.1. Reagents and chemicals

Gold chloride trihydrate (HAuCl₄·4H₂O), sodium borohydride (NaBH₄), silver nitrate (AgNO₃), ascorbic acid, cetanecyl trimethyl ammonium chloride (CTAC), trisodium citrate, hydrogen chloride (HCl, 36%), hydrogen peroxide solution (H₂O₂, 30 wt%), ammonia solution (NH₃·H₂O, 25 wt%), cuprous (II) chloride dihydrate (CuCl₂·2H₂O), sodium hydroxide (NaOH), hydroxylamine hydrochloride (NH₂OH·HCl), sodium dodecyl sulphate (SDS), absolute ethanol, methyl orange (MO), *p*-benzoquinone (PBQ), triethanolamine (TEOA), and *tert*-butyl alcohol (TBA) were all analytical reagent grade and purchased from Sinopharm

Chemical Reagent Co., Ltd (Shanghai, China). Cetyltrimethyl ammonium bromide (CTAB) was obtained from Alfa Aesar. Deionized (DI) water with a resistivity of 18.2 MΩ·cm was used in all the experiments.

2.2. Synthesis of Au NBPs

Au NBPs were prepared using a seed-mediated growth method [40]. Specifically, the citrate-stabilized seed solution was made by adding a freshly prepared, ice-cold NaBH₄ solution (0.01 M, 0.15 mL) into an aqueous solution composed of HAuCl₄ (0.01 M, 0.125 mL), trisodium citrate (0.01 M, 0.25 mL), and DI water (9.625 mL) under vigorous stirring. The resultant seed solution was kept at room temperature for 2.5 h before use. The CTAB growth solution was prepared by sequential addition of HAuCl₄ (0.01 M, 2 mL), AgNO₃ (0.01 M, 0.4 mL), HCl (1 M, 0.8 mL), and ascorbic acid (0.1 M, 0.32 mL) into an aqueous CTAB solution (0.1 M, 40 mL). The seed solution was then added into the growth solution, followed by gentle inversion mixing for 10 s. The reaction solution was left undisturbed overnight at room temperature. The LPRWs of the Au NBP samples grown in the CTAB growth solutions could be varied with different volumes of seed solution. Then the as-grown Au NBP solution (40 mL) of a certain size was centrifuged at 6800 − 7000 rpm for 10 min. The precipitate was re-dispersed in a CTAC solution (0.08 M, 30 mL), which was followed by subsequent addition and mixing of AgNO₃ (0.01 M, 8 mL) and ascorbic acid (0.1 M, 4 mL). The resultant solution was kept in an oven at 60 °C for 4 h, during which Ag was overgrown on the Au nanocrystals to produce bimetallic Au/Ag products. The bimetallic Au/Ag products were then centrifuged at 4000 rpm for 10 min. The precipitate was re-dispersed in CTAB (0.05 M, 30 mL) and left undisturbed overnight at room temperature, and then the supernatant was discarded. The remaining Au/Ag heteronanorods were re-dispersed in water (20 mL). The resultant solution was subsequently mixed gently with NH₃·H₂O (30 wt%, 0.4 mL) and H₂O₂ (0.1 M, 0.3 mL) and kept undisturbed for 4 h to remove Ag. The clear supernatant was carefully taken out and centrifuged at 6800 rpm for 10 min. The Au NBP product was re-dispersed in a CTAB solution (0.01 M, 20 mL) for further use. The synthesized Au NBPs with LPRWs of 765, 785 and 810 nm were named as Au NBP–765, Au NBP–785, and Au NBP–810, respectively.

2.3. Synthesis of Au NRs

Au NRs were also prepared by seed-mediated growth method [37]. Specifically, the seed solution was prepared by adding a freshly prepared, ice-cold NaBH₄ solution (0.01 M, 0.6 mL) into a mixture of HAuCl₄ (0.01 M, 0.25 mL) and CTAB (0.1 M, 9.75 mL). The resultant solution was mixed by rapid inversion for 30 s and then kept at room temperature for 2 h before use. The growth solution was prepared by the sequential addition of HAuCl₄ (0.01 M, 2 mL) and ascorbic acid (0.1 M, 0.32 mL) into CTAB (0.1 M, 40 mL). The seed solution (100 μL) was then added into the growth solution, followed by gentle inversion mixing for 10 s. The reaction solution was left undisturbed overnight at room temperature. The synthesized Au NRs with LPRW at 788 nm were named as Au NR–788.

2.4. Synthesis of jujube-like Au NBP@Cu₂O composites, Au NR@Cu₂O nanobars, and pure Cu₂O

Au NBP@Cu_2O composites were synthesized as follows. Typically, SDS (0.5 g) was dispersed into DI water (50 mL) under stirring. The Au NBP solution (20 mL) mentioned above were concentrated by centrifugation and then dispersed into DI water (2 mL). The concentrated Au NBPs were then added into above SDS solution dropwise. After 10 min, CuCl₂ solution (0.1 M, 500 μL) was added dropwise. After another 10 min, NaOH solution (1 M, 500 μL) was dropped into the mixture, followed by injecting NH₂OH·HCl solution (0.1 M, 840 μL) quickly. The color of the solution changed in 30 s and verified with different Au
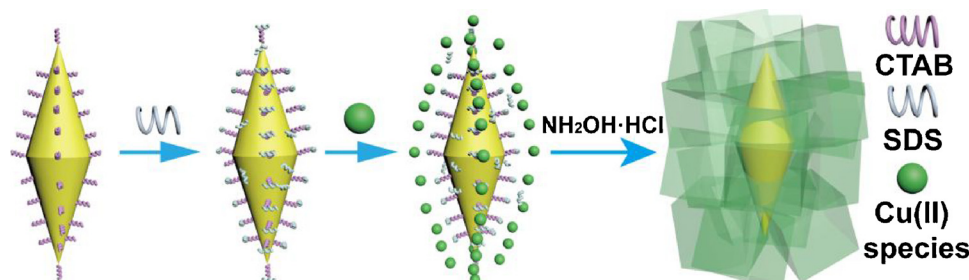
Fig. 1. Schematic illustration of the formation progress of Au NBP@Cu$_2$O composites.

NBP volumes added. The total volume of the reaction solution was kept at 50 mL for all samples. After stirring for 2 h, the products were collected by centrifugation and then washed with DI water and ethanol (1:1) mixture several times. The Au NBP@Cu$_2$O products were finally re-dispersed in ethanol and stored in refrigerator at 4 ^{0}C.

Au NR@Cu$_2$O nanobars were prepared with the same the method mentioned above, except replacing the Au NBP solution with Au NR–788 solution. The optical densities of Au NBPs and Au NRs were kept the same per milliliter.

Pure Cu$_2$O was prepared by the same the method of preparing Au NBP@Cu$_2$O, except replacing the Au NBP solution with DI water during the synthetic process.

2.5. Characterizations

Scanning electron microscopy (SEM) images were taken on a field emission scanning electron microscope (Ultra Plus, Carl Zeiss, Germany) with acceleration voltage of 5 kV. Transmission electron microscopy (TEM) images were taken on a transmission electron microscope (JEM–2100, JEOL, Japan) operated at 200 kV. The high-angle annular dark-field scanning transmission electron microscopy (HAADF-STEM) image, elemental line profiling, and elemental mapping were carried put on an FEI Talos F200X microscope (USA). The crystal structures of the resultant products were characterized by X-ray powder diffraction (XRD) on an Advance D8 instrument (Bruker Corporation, Germany) with Cu Kα (λ = 1.54 Å) radiation at a scanning rate of 6°/ min. Ultraviolet-visible (UV–vis) absorption spectra were recorded by a Lambda 950 UV–vis-NIR spectrophotometer (Perkin-Elmer, USA).

2.6. Photocatalytic activity measurement

The photocatalytic behaviors of all the samples were evaluated by the degradation of MO. Typically, photocatalysts (50 mg) were dispersed into MO aqueous solution (10 mg/mL, 50 mL) under ultrasonic treatment. The solution was stirred for 1 h in the dark to achieve adsorption–desorption equilibrium, and then illuminated under a 300 W Xe arc lamp (PLS-SXE300UV, Beijing Perfect Light Co., Ltd.). The optical power and current are 50 W and 15 A, respectively. The distance between the lamp and the reactor is 20 cm. Every 10 min, aliquots (5 mL) were taken out and centrifuged to remove the photocatalytic particles. The absorption of the supernatant MO solution was determined spectrophotometrically at λ_{max} = 464 nm. To exclude the effect of the plasmonic photothermal conversion, the reactor was kept in a water bath to maintain the system at room temperature.

2.7. Electrochemical impedance spectra (EIS) measurement

The samples with same concentration were collected on cellulose membranes by suction filtration. Before testing, the cellulose membranes were pressed at 10 MPa for 1 min and cut into 0.5 × 0.5 cm pieces. A mixture containing 10 mM K$_3$[Fe(CN)$_6$]/K$_4$[Fe(CN)$_6$] (1:1) and 0.5 M KCl was used as electrolyte, while a Pt foil and Ag/AgCl electrode were used as counter electrode and reference electrode,

respectively. The EIS measurement was performed with an electrochemical workstation (CHI760E, Chenhua, Shanghai, China) in a frequency region from 10 MHz to 100 mHz and an AC amplitude of 5 mV under illumination (λ > 400 nm) at room temperature.

2.8. Reactive species trapping experiment

Typically, PBQ (1 mM), TEOA (1 mM) and TBA (1 mM) were used as ·O$_2^-$, h$^+$ and ·OH scavengers, which were added in the reaction system respectively before photocatalytic activity test. The following steps were the same as the photocatalytic activity measurement.

3. Results and discussion

The core-shelled Au NBP@Cu$_2$O composites were prepared by coating Cu$_2$O on pre-produced Au NBPs as displayed in Fig. 1. Au NBPs were synthesized with CTAB as stabilizing agent, and thus are positive charged. Another surface agent SDS with negative charge acts as coupling agent for positive charged Au NBPs and Cu^{2+} ions in the reaction system. After the addition of reducing agent NH$_2$OH·HCl, Cu (II) can be reduced to Cu (I) and form Cu$_2$O, which will be generally coated on Au NBPs through a heterogeneous nucleation progress.

Fig. 2a–e show SEM images of the Au NBP@Cu$_2$O composites synthesized by introducing 1, 2, 3, 4 and 5 mL of Au NBP solution, which are denoted as Au NBP@Cu$_2$O$_{(1)}$, Au NBP@Cu$_2$O$_{(2)}$, Au NBP@Cu$_2$O$_{(3)}$, Au NBP@Cu$_2$O$_{(4)}$, and Au NBP@Cu$_2$O$_{(5)}$, respectively. Pure Au NBPs used have length/diameter of 110/33 nm and aspect ratio of 3.32 (Fig. S1). The resulting five Au NBP@Cu$_2$O composites have stellated morphology and uniform sizes with lengths/diameters of 263/171, 220/168, 194/135, 182/101 and 170/86 nm, respectively (Table 1). From Au NBP@Cu$_2$O$_{(1)}$ to Au NBP@Cu$_2$O$_{(5)}$, the size of Au NBP@Cu$_2$O decreases and Au NBP cores become more and more visible, indicating the decrease of Cu$_2$O shell thickness. To figure out the formation process of stellated Au NBP@Cu$_2$O composites, pure Cu$_2$O and Au NR@Cu$_2$O were prepared for comparison (Figs. S2 and S3). It can be seen that pure Cu$_2$O has a cubic morphology and Au NR@Cu$_2$O possesses a nanobar-like structure which is also bounded with entire {100} facets like pure Cu$_2$O. The overgrowth of Cu$_2$O on the Au core happens due to the good affinity of Cu$_2$O to Au surface and their comparable crystal symmetry [48]. It is evidenced that the side surface of Au NRs are flat {100} and {110} facets parallel to the length direction, while the sides surface of Au NBPs are {111} facets and periodically stepped {100} facets which occupies one quarter of the whole surface area [36]. The distinct morphology feature of Au NBP@Cu$_2$O stellated polyhedrons must be ascribed to the uniquely stepped {100} facets on the Au NBP core, which disorders the overgrowth of Cu$_2$O particles.

According to previous reports that thin semiconductor shell in metal@semiconductor composites led to a better photocatalytic performance, we then tried to continue to decrease the shell thickness by employing more Au NBPs in Cu$_2$O [48]. But unfortunately, bare Au NBP without Cu$_2$O shell occur in the Au NBP@Cu$_2$O composites with the increasing Au NBP concentrations (Fig. S4). This may be because the relatively insufficient cuprous ions cannot wrap excess Au NBPs and
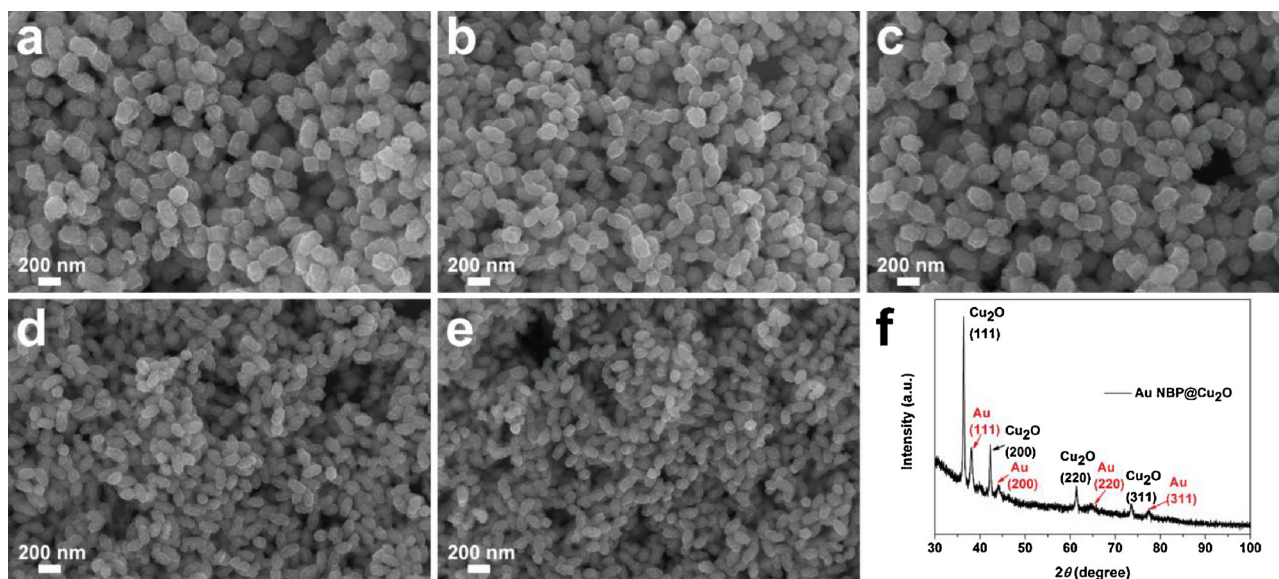
Fig. 2. (a–e) SEM images of Au NBP@Cu$_2$O$_{(1)}$, Au NBP@Cu$_2$O$_{(2)}$, Au NBP@Cu$_2$O$_{(3)}$, Au NBP@Cu$_2$O$_{(4)}$, and Au NBP@Cu$_2$O$_{(5)}$ composites synthesized with 1, 2, 3, 4 and 5 mL of Au NBP solution, respectively. (f) XRD pattern of Au NBP@Cu$_2$O$_{(5)}$ composites.

Table 1
Sizes, Cu$_2$O shell thicknesses, TPRWs and LPRWs of Au NBPs and all of the Au NBP@Cu$_2$O samples.

Sample	Length (nm)	Diameter (nm)	Cu$_2$O shell thickness (nm)	TPRW (nm)	LPRW (nm)
Au NBP–810	110	33	–	510	810
Au NBP–810@Cu$_2$O$_{(1)}$	263	171	70	–	1296
Au NBP–810@Cu$_2$O$_{(2)}$	220	168	55	655	1278
Au NBP–810@Cu$_2$O$_{(3)}$	194	135	44	648	1270
Au NBP–810@Cu$_2$O$_{(4)}$	182	96	37	642	1261
Au NBP–810@Cu$_2$O$_{(5)}$	170	86	30	639	1251
Au NBP–785	98	32	–	510	785
Au NBP–785@Cu$_2$O$_{(1)}$	250	177	70	–	1247
Au NBP–785@Cu$_2$O$_{(2)}$	208	131	55	650	1240
Au NBP–785@Cu$_2$O$_{(3)}$	185	112	43	646	1230
Au NBP–785@Cu$_2$O$_{(4)}$	167	103	34	639	1220
Au NBP–785@Cu$_2$O$_{(5)}$	158	94	30	635	1207
Au NBP–765	93	32	–	515	765
Au NBP–765@Cu$_2$O$_{(1)}$	243	166	76	–	1222
Au NBP–765@Cu$_2$O$_{(2)}$	203	126	55	660	1207
Au NBP–765@Cu$_2$O$_{(3)}$	181	106	43	655	1194
Au NBP–765@Cu$_2$O$_{(4)}$	164	100	34	648	1180
Au NBP–765@Cu$_2$O$_{(5)}$	155	96	30	643	1168

therefore leave bare Au NBPs alone. Considering the cost of gold sources, it is acceptable to obtain Au NBP@Cu$_2$O composites with less amounts of Au NBPs as long as they still show significantly enhanced photocatalytic performance. Based on this, only the above five Au NBP@Cu$_2$O composite samples synthesized by using 1, 2, 3, 4 and 5 mL of Au NBP solution were characterized and their performances were evaluated in the following work.

XRD pattern for Au NBP@Cu$_2$O in Fig. 2f shows both Au and Cu$_2$O peaks and demonstrates there are no other impurities, such as CuO, in Au NBP@Cu$_2$O composites (take Au NBP@Cu$_2$O$_{(5)}$ as an example). The two series of four diffraction peaks of (111), (200), (220) and (311) planes correspond to pure Cu$_2$O (JCPDS, 65–3288) and cubic–phase Au (JCPDS, 5–667), respectively [49]. The intensities of Au NBP peaks are lower than those of Cu$_2$O because Au NBPs are located inside Cu$_2$O shell. For Cu$_2$O, the obviously stronger peak intensity at (111) plane may reveal the exposed {111} facets of Cu$_2$O [48].

To investigate the Au NBP@Cu$_2$O morphology clearly, TEM images of the five Au NBP@Cu$_2$O samples were obtained and are shown in

Fig. 3a–e. It is obvious that each Au NBP@Cu$_2$O particle only contains one individual Au NBP core. Interestingly, the Au NBP@Cu$_2$O composite looks extremely like the jujube, as shown in the inset of Fig. 3a. The stellated Cu$_2$O shell is like the jujube pulp while the Au NBP looks like the jujube pit. The Au NBP cores become more visible when more Au NBPs are introduced, and the Cu$_2$O shell thicknesses are 70, 55, 44, 37 and 30 nm for Au NBP@Cu$_2$O$_{(1)}$, Au NBP@Cu$_2$O$_{(2)}$, Au NBP@Cu$_2$O$_{(3)}$, Au NBP@Cu$_2$O$_{(4)}$, and Au NBP@Cu$_2$O$_{(5)}$, respectively, which are in consistent with SEM results. Fig. 3f shows the high resolution TEM (HRTEM) image of Au NBP@Cu$_2$O composite, where the dashed line represents the interface region between Au NBP core and Cu$_2$O shell. The lattice spacing of 2.46 Å corresponds to (111) plane of Cu$_2$O and the lattice spacing of 2.38 Å corresponds to (111) plane of Au [49], agreeing well with the XRD results above. Besides, the paralleled (111) planes of Cu$_2$O to {111} facets of Au NBP confirms the overgrowth of Cu$_2$O on Au NBP core, which can be attributed to their relatively low lattice mismatch of 4.5% [50].

The core-shelled structure of Au NBP@Cu$_2$O composites was further demonstrated by HAADF-STEM analysis. The Au NBP@Cu$_2$O$_{(5)}$ composites were taken as respective sample (Fig. 4a). Fig. 4b shows elemental line profiles crossing a representative Au NBP@Cu$_2$O particle. The Au signal appears in the middle, while the Cu and O signals appear over the whole cross-section of the Au NBP@Cu$_2$O particle, undoubtedly revealing the Au core@Cu$_2$O shell structure. Fig. 4c displays the HAADF-STEM image of the signal Au NBP@Cu$_2$O particle, confirming the core-shelled feature visually. The elemental mappings of this single Au NBP@Cu$_2$O particle in Fig. 4d–f verifies the distribution of Au, Cu and O elements, where Au element is distributed as a bi-pyramid like core and Cu and O elements are distributed as the shell around the Au NBP core. The above results together indicate the successful synthesis of core-shelled Au NBP@Cu$_2$O composites.

In order to investigate the influence of Au NBP cores with different aspect ratios on the geometry of Au NBP@Cu$_2$O composites, we also synthesized Au NBP@Cu$_2$O composites by using Au NBP cores with aspect ratios of 2.88 and 3.07, which have lengths/diameters of 93/32 nm and 98/32 nm and LPRWs of 765 and 785 nm, respectively (Fig. S5a and S6a). For the two Au NBP–765@Cu$_2$O and Au NBP–785@Cu$_2$O composites, they both maintain jujube-like features, and Cu$_2$O shell thickness decreases with increasing Au NBP concentrations, just like that of Au NBP–810@Cu$_2$O composites (Fig. S5b–f and S6b–f). The lengths/diameters/shell thicknesses are 243/166/73 nm, 203/126/
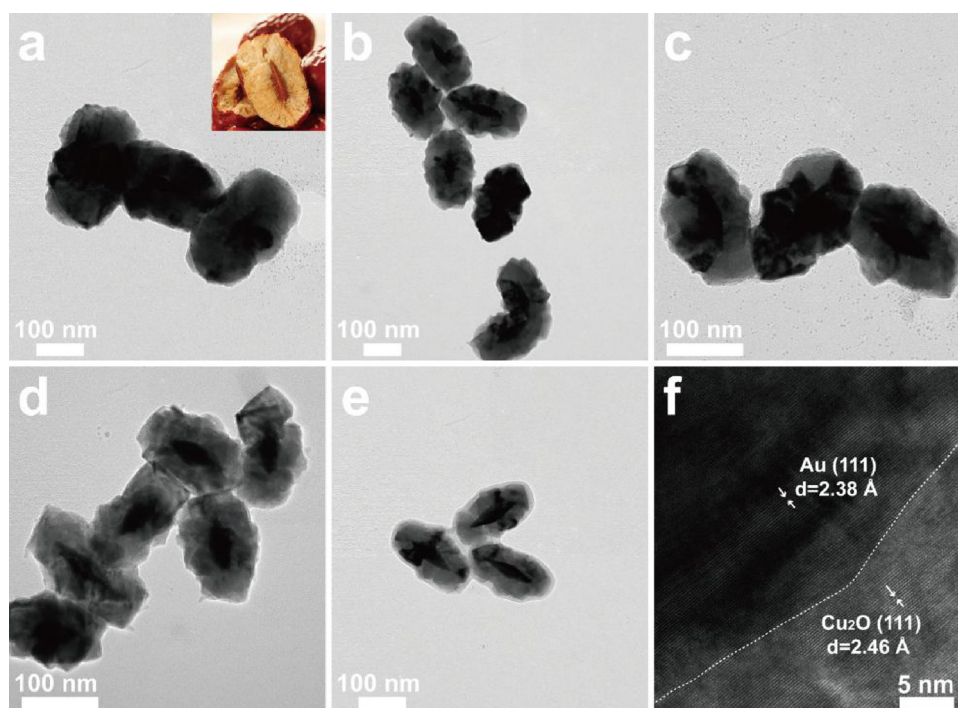
Fig. 3. (a–e) TEM images of Au NBP@Cu$_2$O$_{(1)}$, Au NBP@Cu$_2$O$_{(2)}$, Au NBP@Cu$_2$O$_{(3)}$, Au NBP@Cu$_2$O$_{(4)}$, and Au NBP@Cu$_2$O$_{(5)}$ composites, respectively. (f) HRTEM image of the interface region on Au NBP@Cu$_2$O$_{(5)}$ composite. The dashed line represents the interface between Au NBP and Cu$_2$O.

53 nm, 181/106/42 nm, 164/100/34 nm, and 155/96/31 nm for Au NBP–765@Cu$_2$O composites, and 250/177/76 nm, 208/131/55 nm, 185/112/43 nm, 167/103/34 nm, 158/94/30 nm for Au NBP–785@Cu$_2$O composites, when 1, 2, 3, 4 and 5 mL of Au NBP solution were used, respectively (Table 1). It is interestingly found that the Cu$_2$O shell thicknesses for the three Au NBP–765@Cu$_2$O, Au NBP–785@Cu$_2$O and Au NBP–810@Cu$_2$O composites are almost the same when using Au NBP solution with same concentrations. This may be resulted from a check and balance between the decreasing Au numbers and increasing Au sizes determined by the aspect ratios.

The optical properties were evaluated by UV–vis absorption spectra to observe the light response of Au NBP@Cu$_2$O photocatalysts. Usually, Au NBPs exhibit a strong longitudinal dipolar plasmon peak in low-energy region and two or three weak peaks in the higher-energy region.
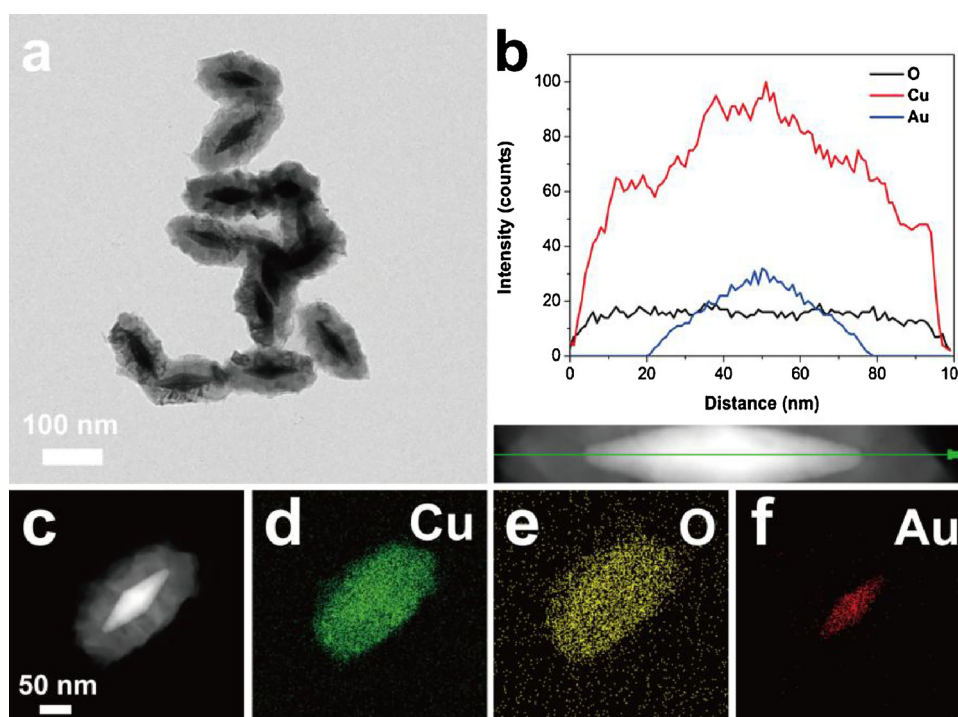

Fig. 4. (a) TEM image of Au NBP@Cu$_2$O$_{(5)}$ composites. (b) Elemental profiles of a representative Au NBP@Cu$_2$O$_{(5)}$ particle. (c) HAADF-STEM image of the single Au NBP@Cu$_2$O$_{(5)}$ particle. (d–f) Elemental maps of Cu, O and Au on the particle from (c), respectively.
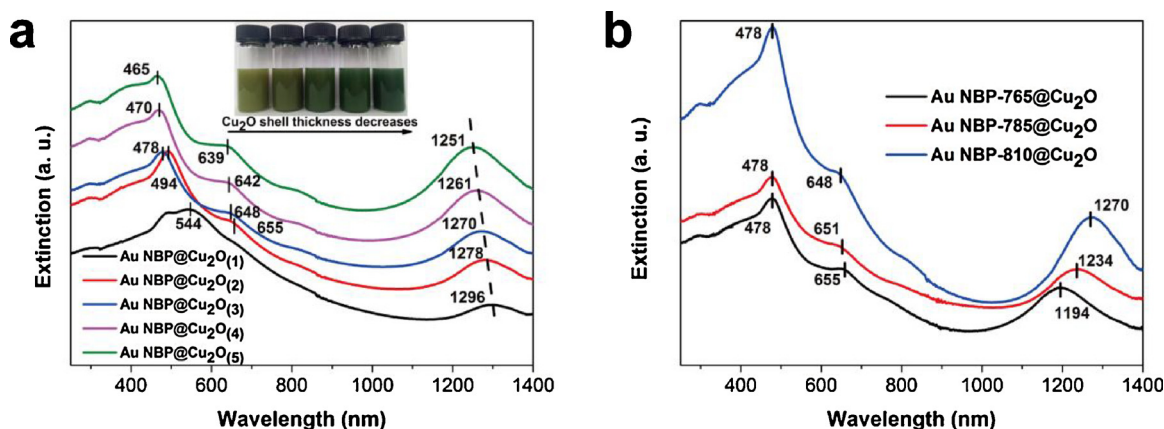
Fig. 5. (a) UV–vis absorption spectra and corresponding photographs of Au NBP@Cu$_2$O$_{(1)}$, Au NBP@Cu$_2$O$_{(2)}$, Au NBP@Cu$_2$O$_{(3)}$, Au NBP@Cu$_2$O$_{(4)}$ and Au NBP@Cu$_2$O$_{(5)}$ composites synthesized with 1, 2, 3, 4 and 5 mL of Au NBP–810 solution, respectively. (b) Comparison of UV–vis absorption spectra for Au NBP@Cu$_2$O composites synthesized with 3 mL of Au NBP–765, Au NBP–785, and Au NBP–810 solution, respectively. For particle stability reason, spectral analysis was performed in ethanol.

The weak peaks arise from the transverse dipolar plasmon mode, and longitudinal higher-order plasmon modes which depend on the size of Au NBPs [40]. Accordingly, for Au NBP–810, the strong peak at 810 nm is attributed to longitudinal dipolar plasmon mode and the week peak at 510 nm is attributed to the transverse dipolar plasmon mode, whereas the peak at 577 nm is attributed to the longitudinal higher-order plasmon mode and it will disappear with the decrease of Au NBP size. Fig. 5a shows UV–vis absorption spectra of the five Au NBP–810@Cu$_2$O composites, respectively. As described above, Cu$_2$O shell becomes thinner with more amounts of Au NBPs introduced, which here is displayed visibly by the color changes of Au NBP@Cu$_2$O solutions varying gradually from yellow-green to dark-green (see the inset in Fig. 5a). For the five Au NBP@Cu$_2$O composites, the absorption band in the range of 465–544 nm derives from the Cu$_2$O absorption, which shows blue-shift with the decrease of Cu$_2$O shell thickness, in other words, with the decrease of the Au NBP@Cu$_2$O particle size, due to the particle size-dependent light scattering feature of Cu$_2$O [50]. Because of the high refractive index of Cu$_2$O (n ≈ 2.7) surrounding Au NBP core [51], the LPRW of Au NBPs has a large red-shift from 810 nm for bare Au NBPs to 1251–1296 nm for Au NBP@Cu$_2$O composites, while the TPRW shows a relatively smaller red-shift from 510 nm for bare Au NBPs to 639–655 nm for Au NBP@Cu$_2$O composites (Table 1). Both the LPRW and TPRW of Au NBP blue shift with decreasing Cu$_2$O shell thickness, as a result of the decreasing refractive index around Au NBPs. The peaks at LPRWs are more distinct than those at TPRWs for Au NBP@Cu$_2$O composites because of the initial strong SPR effect of Au NBPs in longitudinal axis. The TPRW occurs only when relatively thinner Cu$_2$O shell is encapsulated over Au NBPs, so that Au NBP@Cu$_2$O$_{(1)}$ composites display no TPRWs, just because of the interference of light scattering from their too thick Cu$_2$O shell. Furthermore, the UV–vis absorption spectra of Au NBP–765@Cu$_2$O and Au NBP–785@Cu$_2$O composites were detected, and the results are shown in Fig. S7 and S8, respectively. Both of them show Cu$_2$O shell thickness-dependent optical properties like that of the Au NBP–810@Cu$_2$O composites. Specifically, the LPRW of Au NBP–765 red shifts from 765 to 1168–1222 nm and the TPRW red shifts from 515 to 643–660 nm for Au NBP–765@Cu$_2$O composites, while the LPRW of Au NBP–785 red shifts from 785 to 1207–1247 nm and the TPRW red shifts from 510 to 635–650 nm for Au NBP–785@Cu$_2$O composites (Table 1). The results above reveal the introduction of Au NBPs can extend the light absorption of Cu$_2$O to near-infrared region. The character of adjustable light absorption for Au NBP@Cu$_2$O composites can endow them with optimal photocatalytic performance under light irradiation of specific wavelength. This will provide a guidance for people to design specific Au NBP@Cu$_2$O composites according to practical requirement.

We then compared the UV–vis spectra of the three Au NBP–810@Cu$_2$O, Au NBP–785@Cu$_2$O and Au NBP–765@Cu$_2$O composites all synthesized with 3 mL of Au NBP solution respectively (Fig. 5b), whose Cu$_2$O shell thicknesses are nearly the same (44, 43 and 43 nm, respectively) as described above. The absorption band at 478 nm from Cu$_2$O absorption is fixed at the same position for the three samples, owing to the same geometry of Cu$_2$O shell. The LPRWs are located at 1194, 1234 and 1270 nm and the TPRWs are located at 655, 651 and 648 nm for Au NBP–765@Cu$_2$O, Au NBP–785@Cu$_2$O, and Au NBP–810@Cu$_2$O composites, respectively. Obviously, the LPRW red shifts to longer-wavelength region with lager aspect ratios of Au NBPs used. Additionally, we compared the UV–vis spectra between Au NBP@Cu$_2$O and Au NR@Cu$_2$O, when using Au NBP–785 and Au NRs–788 cores with close LPRW (Fig. S9). It is apparent that the Au NBP–785@Cu$_2$O can make a much larger red-shift (462 nm) than that of Au NR–788@Cu$_2$O (300 nm). This indicates it is better to employ Au NBP cores in the fabrication of Au@Cu$_2$O composites to achieve a wider spectral response. Furthermore, UV–vis diffuse reflectance spectroscopy (DRS) measurement was carried out (Fig. S10), as a method to investigate the interaction between photocatalysts and light directly [15]. Compared with pure Cu$_2$O, Au NBP@Cu$_2$O composites show notably enhanced absorption at 550–700 nm region, which is assigned to band-edge absorbance of Au NBPs. So it is firmly believed that the introduction of Au NBPs into Cu$_2$O can improve and extend light absorption for Cu$_2$O.

The photocatalytic activities of Au NBP@Cu$_2$O composites were evaluated by the photodegradation of MO under illumination (λ > 400 nm). There is no degradation of MO when in the absence of any catalysts (Fig. S11). Fig. 6a shows the photocatalytic behaviors of pure Cu$_2$O and the five Au NBP–810@Cu$_2$O composites, respectively. All of the five Au NBP@Cu$_2$O composites exhibit better photocatalytic activities than pure Cu$_2$O. From Au NBP@Cu$_2$O$_{(1)}$ to Au NBP@Cu$_2$O$_{(5)}$, the photocatalytic performance generally gets better, revealing Au NBP@Cu$_2$O with thinner Cu$_2$O shell possesses better photocatalytic activity. This is because thick Cu$_2$O shell means a long distance for photogenerated holes/electrons to migrate to the surface of Cu$_2$O to participate in photocatalysis and thus causes weak photocatalytic efficiency. Fig. 6b presents the corresponding histogram to Fig. 6a, from which the degradation efficiency of pure Cu$_2$O and Au NBP@Cu$_2$O composites can be obtained directly. That is only 2.45% of MO degraded after 60 min in the presence of pure Cu$_2$O, but 100% of MO is degraded in the presence of Au NBP@Cu$_2$O$_{(5)}$ composites. The contents of total organic carbon are 25.6 and 7.83 mg/L before and after the photodegradation, respectively, indicating the efficient photodegradation of MO by using Au NBP@Cu$_2$O composites. Moreover,
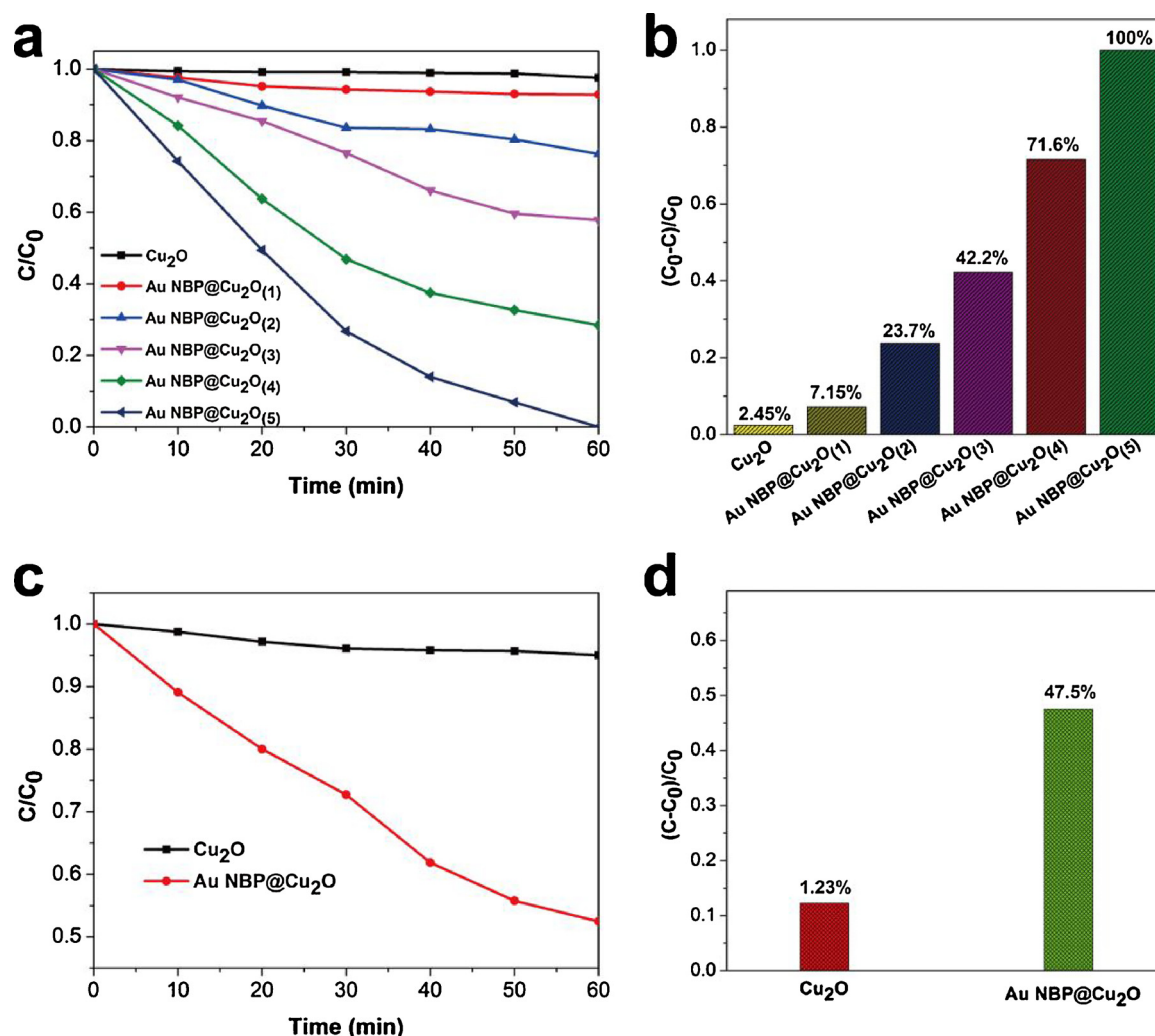
Fig. 6. (a) Photocatalytic degradation of MO in the presence of pure Cu_2O and five Au NBP–810@Cu_2O composites under illumination ($\lambda > 400$ nm), respectively. (b) The histogram corresponding to (a). (c) Photocatalytic degradation of MO in the presence of pure Cu_2O and Au NBP@$Cu_2O_{(5)}$ composites under illustration ($\lambda > 700$ nm), respectively. (d) The histogram corresponding to (c).

photocatalytic activities of pure Cu_2O and Au NBP@$Cu_2O_{(5)}$ were detected under illumination ($\lambda > 700$ nm), as shown in Fig. 6c. According to the analysis of UV–vis spectra results, Au NBP@$Cu_2O_{(5)}$ composites show enhanced and extended light absorption to near-infrared region, revealing their potential in photocatalytic activity under near-infrared light. Just as expected, the Au NBP@$Cu_2O_{(5)}$ composites indeed exhibit superior photocatalytic performance to pure Cu_2O under illumination ($\lambda > 700$ nm). The corresponding histogram in Fig. 6 d intuitively reveals the much better photocatalytic behavior of Au NBP@$Cu_2O_{(5)}$ composites with 47.5% photodegradation of MO compared with only 1.23% over pure Cu_2O. Because the illumination ($\lambda > 700$ nm) cannot excite Cu_2O to generate hole/electron pairs, the superior photocatalytic performance of Au NBP@Cu_2O should be contributed to the SPR effect of Au NBP cores, which generate hot electrons to inject into Cu_2O shell and achieve the photodegradation of MO. Based on this, we can explain why the thin shell in Au NBP@$Cu_2O_{(5)}$ can achieve better photocatalytic performance under illumination ($\lambda > 700$ nm). That is thin shell can make full utilization of the plasmon-enhanced electric field and reduce recombination of SPR-initiated carriers in Cu_2O. For comparison, the photodegradation in the presence of pure Au NBPs and Au NBPs mix with Cu_2O were determined (Fig. S11). Neither pure Au NBPs nor Au NBPs mix with Cu_2O exhibits photocatalytic performance, indicating the SPR effect functions only when there is a close connection between Au NBP and Cu_2O. Besides,

the inactivity of Au NBPs mix with Cu_2O demonstrates that photothermal effect cannot cause photodegradation of MO. We should note that the photocatalytic experiments under illumination with monochromatic wavelengths in present study were absent because we failed to buy the LED lamp with monochromatic wavelength ($\lambda > 1000$ nm). We have only carried out photocatalytic experiments under monochromatic light illumination with wavelengths at 420, 550 and 700 nm, respectively, by using LED lamps as cold light sources. It was found that the photocatalytic ability under illumination ($\lambda = 550$ nm) was the highest while the photocatalytic ability under illumination ($\lambda = 700$ nm) is slightly lower. This is because the illumination ($\lambda = 550$ nm) can excite Cu_2O shell to generate holes and electrons and may also excite the SPR effect of Au NBPs core, whereas the illumination ($\lambda = 700$ nm) can only excite the transverse plasmon resonance of Au NBP core and generate hot electrons to induce photodegradation. The photocatalytic activity under illumination ($\lambda = 400$ nm) is the lowest because it can only excite Cu_2O shell with low light absorption. Considering the photocatalytic activities under the two monochromatic light ($\lambda = 550$ and 700 nm) are nearly the same, we can predict that the photocatalytic activity under monochromatic light with wavelength close to LPRW must be much higher because the intensity of longitudinal plasmon resonance of Au NBPs is much higher than those on transverse axis [40]. This part is not emphasized here in order to avoid misunderstanding and we will try to achieve this in future work. We
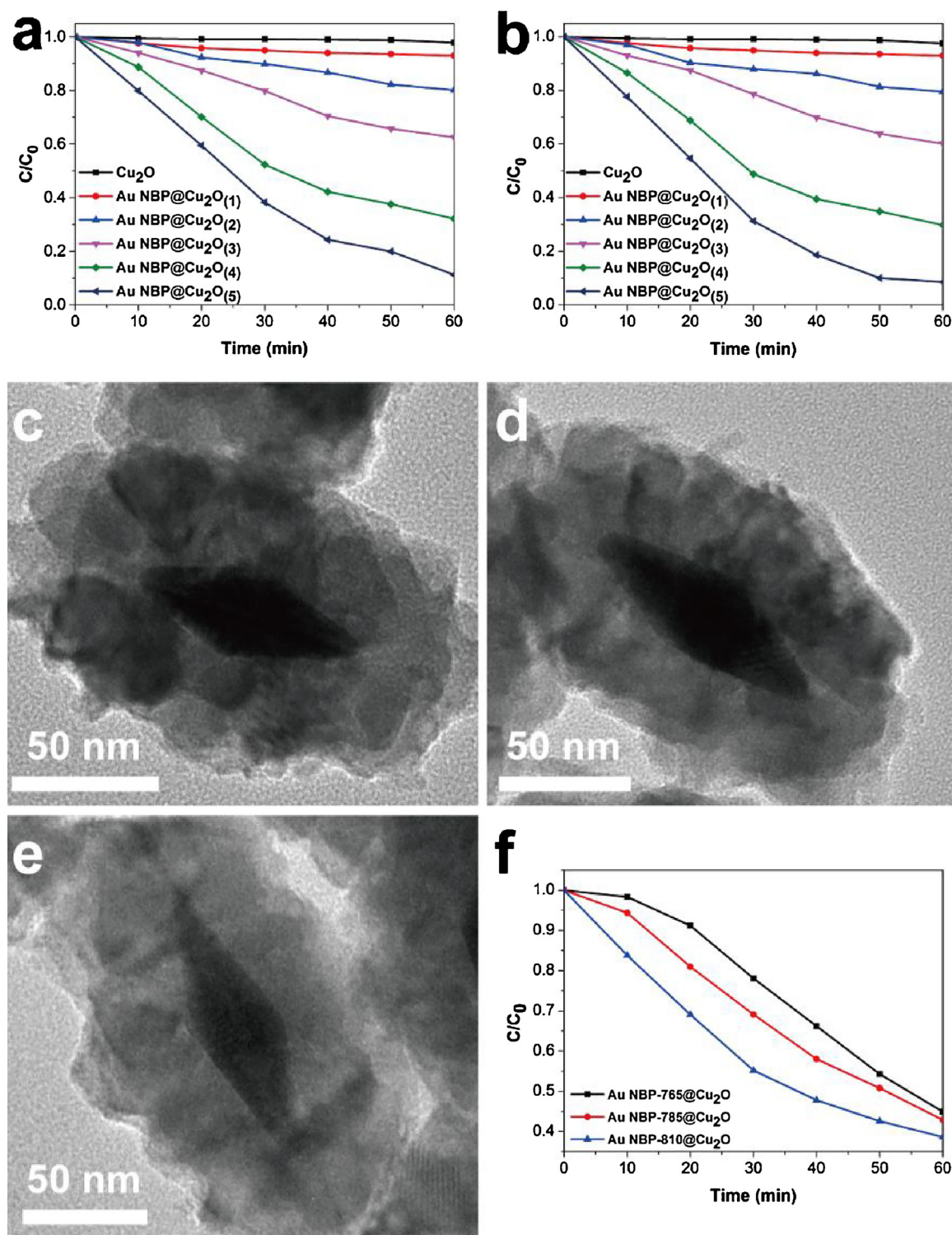
Fig. 7. (a) Photocatalytic degradation of MO in the presence of pure Cu_2O and five Au NBP–765@Cu_2O composites, respectively. (b) Photocatalytic degradation of MO in the presence of pure Cu_2O and five Au NBP–785@Cu_2O composites, respectively. (c–e) TEM images of Au NBP–765@Cu_2O, Au NBP–785@Cu_2O and Au NBP–810@Cu_2O composites which were all synthesized by using 3 mL of Au NBP solution, respectively. (d) Photocatalytic degradation of MO in the presence of the three samples in (c), respectively. Here the concentration of photocatalyst solution was kept at 1.5 g/L.

believe it is an energy-saving strategy in practical applications that people can choose to design specific Au NBP@Cu_2O composites with LPRW close to the wavelengths of monochromatic light sources.

Since it was determined that Au NRs with appropriate aspect ratio could achieve optimum photocatalytic behavior for Au NR@Cu_2O composites [41], we expected the similar regularity for our Au

NBP@Cu_2O composites and the comparison of photocatalytic activities for Au NBP–765@Cu_2O, Au NBP@Cu_2O–785 and Au NBP@Cu_2O–810 composites were carried out. Fig. 7a and b show the photocatalytic activities of Au NBP–765@Cu_2O and Au NBP@Cu_2O–785 composites, respectively. Both of them exhibit better photocatalytic performances than pure Cu_2O. With the decrease of Cu_2O shell thickness, both of the

Au NBP–765@Cu₂O and Au NBP@Cu₂O–785 composites exhibit generally improved photocatalytic behavior from Au NBP@Cu₂O₍₁₎ to Au NBP@Cu₂O₍₅₎, just like that of Au NBP–810@Cu₂O composites. Fig. 7c–e presents the TEM images of three Au NBP–765@Cu₂O, Au NBP–785@Cu₂O, and Au NBP–810@Cu₂O samples all synthesized with 3 mL of Au NBP solution corresponding to Fig. 5b, which have similarly stellated structures and Cu₂O shell thicknesses (43, 43 and 44 nm, respectively). Under the same condition, the photocatalytic activities of MO degradation over the three photocatalysts are in an order of Au NBP–810@Cu₂O > Au NBP–785@Cu₂O > Au NBP–765@Cu₂O (Fig. 7f). Based on the condition of similar geometry of Cu₂O shell, the aspect ratio of Au NBP must be responsible for the different photocatalytic performances of the three composites. With the increasing aspect ratio, the ratio of high energy facet (stepped {100}) to low energy facet ({111}) is changing, which may alter the distribution of active sites on Au NBP@Cu₂O. In addition, the photocatalytic activity of Au NR@Cu₂O prepared with the same method was evaluated and the results are shown in Fig. S13. It can be seen that negligible MO is degraded in the presence of Au NR@Cu₂O composites. This is because the Au NR@Cu₂O are bounded by Cu₂O shell with entire {100} facets, which are inactive and have a high energy barrier that can also hinder hot electrons from Au NBPs to their surface to achieve photodegradation [52]. Based on the above, we can estimate that the aspect ratio of Au NBPs and the morphology of Cu₂O shell are also two important factors to influence the photocatalytic activity of Au@Cu₂O composites, which need our further exploration in the future work.

The stability is also an important indicator to evaluate the quality of photocatalysts [53]. The cycling photocatalytic experiments were carried out as shown in Fig. 8a. The photocatalytic efficiency is slightly decreased after four cycles but still maintains a high value with 94.2% degradation of MO (Fig. 8b), revealing the excellent stability of Au NBP@Cu₂O composites in the photocatalytic applications. Besides, SEM images and XRD pattern of Au NBP@Cu₂O photocatalysts after photocatalytic experiments were obtained (Fig. S14). From the SEM images, we can find the morphologies of the five Au NBP@Cu₂O composites after photocatalytic reaction keep unchanged. The XRD pattern also indicates that no impurities such as CuO occur in Au NBP@Cu₂O composites after photocatalysis. Additionally, photographs in Fig. S15 presents the change of pure Cu₂O and Au NBP@Cu₂O solutions after photocatalytic reaction and continued to be placed after one week. The color of Au NBP@Cu₂O solution maintains unchanged, whereas the color of Cu₂O solution becomes black, indicating the generation of CuO in pure Cu₂O particles. Thus, it is undoubted that the introduction of Au NBPs in Cu₂O can significantly improve the stability of Cu₂O.

Based on the above results, the mechanism for enhanced photocatalytic behavior of Au NBP@Cu₂O composites was proposed. Before this, it is necessary to discuss the facets of Au NBP core and Cu₂O shell because different facets have distinct work functions, which determines the direction of charge carrier migration between Au NBP core and Cu₂O shell. It has been demonstrated the facets of Cu₂O with lower energy, like {100} and {111} facets, can be easily formed at the beginning stage of the particle formation while {110} facets with higher surface energy formed very slowly after 1 h or longer time [54]. We have observed the intermediate products obtained at different time (1, 3 and 10 min) during the formation process of Au NBP@Cu₂O composites in our study and found that the core-shelled Au NBP@Cu₂O composites occurred very fast even in 1 min, only with smaller size than that of final Au NBP@Cu₂O products. Hence, we can speculate that the facets of Cu₂O shell could be {100} or {111} facets or the mix of them. According to Huang's researches, Cu₂O prefers epitaxial growth over Au core to form monocrystal shell because of the relatively small lattice mismatch between Au and Cu₂O [55–58]. Pure Au NBPs are penta-fold twinned around the growth axis and possess {111} facets and stepped {100} facets which possess nearly one quarter of the whole surface area [36]. From the TEM image (Fig. 3f), we can see that the {111} planes of Cu₂O are parallel to {111} facets of Au NBP core. Besides, cubic structures in the vertex of Cu₂O shell can be seen in several Au NBP@Cu₂O particles in TEM images (Fig. S16a – c), indicating the {100} facets of Cu₂O. Thus, it is reasonable to conclude that the Cu₂O shell has {100} and {111} facets which are parallel to {100} and {111} facets of Au NBPs, respectively. Because the work functions for {100} and {111} facets of Au NBPs are 5.07 and 5.11 eV [59,60] and the work functions for {100} and {111} facets of Cu₂O are 7.247 and 4.833 eV, respectively [61,62], Schottky junction can be formed between Au NBP core and {100} facets of Cu₂O. As a result, the holes in (100) planes of p-type Cu₂O can migrate from Cu₂O to Au NBP core, therefore reducing the recombination of photogenerated holes and electrons in Cu₂O shell. This is also the reason that Au NBP@Cu₂O composites exhibit much better stability than pure Cu₂O, just due to the reduction of these oxidizing holes in their Cu₂O shell.

Based on the above analysis, the schematic illustration of possible mechanism for MO photodegradation over Au NBP@Cu₂O composites is presented in Fig. 9. Under illumination ($\lambda > 400$ nm), Cu₂O is excited to generate holes and electrons. For pure Cu₂O, a small parts of hole/electron pairs participate in photocatalytic reaction while most of them recombine quickly. But in the existence of Au NBPs, the photogenerated holes can migrate from Cu₂O to Au NBP rapidly through the Schottky junction between Au NBP and {100} facets of Cu₂O, facilitating separation of holes and electrons and giving a force to the migration of holes on Cu₂O. Meanwhile, Au NBPs have super strong SPR effects because of their unique structure with speculate tips, which on one hand enhance the light absorption for Cu₂O shell and on the other
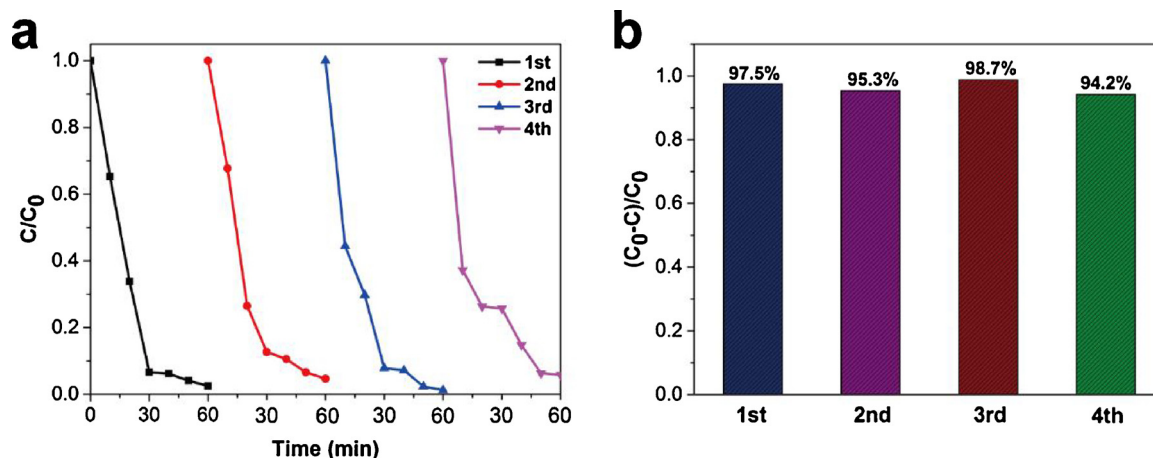

Fig. 8. (a) Cycling runs in photocatalytic degradation of MO in the presence of Au NBP@Cu₂O composites under light irradiation ($\lambda > 400$ nm). (b) The histogram corresponding to (a).
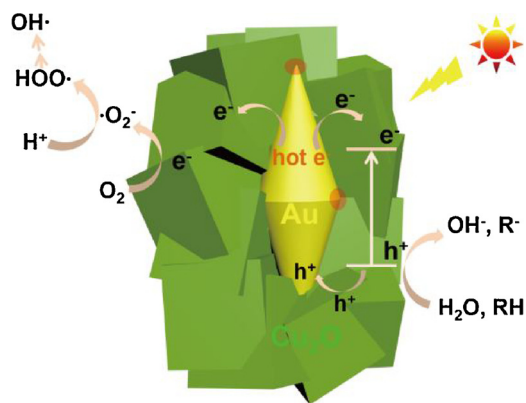
Fig. 9. Schematic illustration of possible mechanism for MO photodegredation over Au NBP@Cu$_2$O composites under illumination (λ > 400 nm).

hand generate plentiful hot electrons to inject into the {111} facets of Cu$_2$O shell [58,63]. After the holes and electrons transfer to the Cu$_2$O surface, the electrons will react with O$_2$ molecules in the solution to form reactive ·O$_2^-$ species and then produce ·OH species via multiple-electron reduction reaction to participate the degradation of MO, while the holes can directly oxidize MO because the energy level of valence band of Cu$_2$O is more positive than that of the highest occupied molecular orbital (HOMO) of MO [64]. The mechanism we proposed here emphasizes the Au NBP core functions like hole sinks, and this is different from those reported in previously numerous studies which all showed that Au cores are used as electron sinks. When under illumination (λ > 700 nm), Cu$_2$O cannot be excited and only the LSPR of Au NBPs can be induced and generate significant amounts of hot electrons which will inject into Cu$_2$O shell and therefore achieve photodegradation. Several previous researches have demonstrated this hot electron mechanism and confirmed that Au nanocrystals with sharp structures exhibited much stronger SPR intensities than conventional Au nanoparticles [40,43,65]. Lastly, we should mention that the holes on the Au NBP core may be not able to participate the photodegradation because the Cu$_2$O shell of Au NBP@Cu$_2$O is measured to be nonporous. The BET areas for pure Cu$_2$O and Au NBP@Cu$_2$O composites are 5.48 and 7.38 m^2/g, respectively, displaying a much small surface area. This is expected because Cu$_2$O prefers to form monocrystal shell rather than amorphous and porous structure on noble metals, which can be also demonstrated in our study (Fig. S16d). Some researches showed that the monocrystal shell was beneficial for accelerating charge transfer between noble metals and Cu$_2$O shell and therefore improving the photocatalytic performance, while some researches indicated that the holes or electrons accumulated on noble metal core could lead to low

photocatalytic efficiency. This may be a double-edged sword for the design of the core-shelled Au@Cu$_2$O composite photocatalysts, and this needs our further exploration.

The reactive species trapping experiment was employed to confirm the reactive species (·O$_2^-$, h$^+$ and ·OH) in the photocatalytic process under illumination (λ > 400 nm). PBQ, TEOA and TBA are common regents as ·O$_2^-$, h$^+$ and ·OH scavengers, respectively [66]. The results in Fig. 10a demonstrates that ·O$_2^-$ and h$^+$ are main reactive species in the photodegradation of MO for our synthesized Au NBP@Cu$_2$O photocatalyst. Both Cu$_2$O shell and Au NBP are excited under illumination (λ > 400 nm) and abundant holes and electrons are generated, which breed reactive species. The ·OH species is relatively difficult to occur because of the unmatched band position between Cu$_2$O and MO. This result is consist well with the above photocatalysis mechanism. Furthermore, the EIS measurement was carried out as a tool to study the interfacial carrier transfer. It has been reported that the radius of the semicircle in a Nyquist plot at high frequency reveals the carrier transfer resistance when moving across the solid–liquid interface [67]. As sown in Fig. 10 b, the Nyquist plot corresponding to Au NBP@Cu$_2$O has a smaller radius of semicircle in the high-frequency region than that of pure Cu$_2$O under illumination (λ > 400 nm), revealing the lower charger transfer resistance in Au NBP@Cu$_2$O composites. This confirms that the introduction of Au NBP in Cu$_2$O can accelerate carrier transfer, which may be one of the reasons that causes enhanced photocatalytic performance.

4. Conclusion

In summary, we have developed a simple approach to improve the photocatalytic performance of Cu$_2$O, through introducing Au NBPs and fabricating core-shelled Au NBP@Cu$_2$O composites. The geometry of the obtained Au NBP@Cu$_2$O composites can be adjusted by changing the Cu$_2$O shell thickness or aspect ratios of Au NBP cores. Accordingly, the light absorption of Cu$_2$O is improved and tunable from visible to near-infrared region with the change of geometry. As expected, Au NBP@Cu$_2$O composites exhibit much better photocatalytic activity than pure Cu$_2$O under both visible and near-infrared light. The introduction of Au NBP plays significant roles in enhancing the photocatalytic activity of Au NBP@Cu$_2$O. On one hand, the Schottky junction formed between Au NBP and the {100} facets of Cu$_2$O shell can drive holes migrate from Cu$_2$O to Au NBP, leading to efficient separation of holes and electrons on Cu$_2$O. On the other hand, the SPR effect from Au NBPs can extend the light response for Cu$_2$O and at the same time generate abundant hot electrons to inject in Cu$_2$O to enhance the photocatalytic efficiency. Owing to the reduction of holes in Cu$_2$O, Au NBP@Cu$_2$O composites also show significantly improved stability than pure Cu$_2$O. Furthermore, we also find the aspect ratios of Au NBP cores as well as
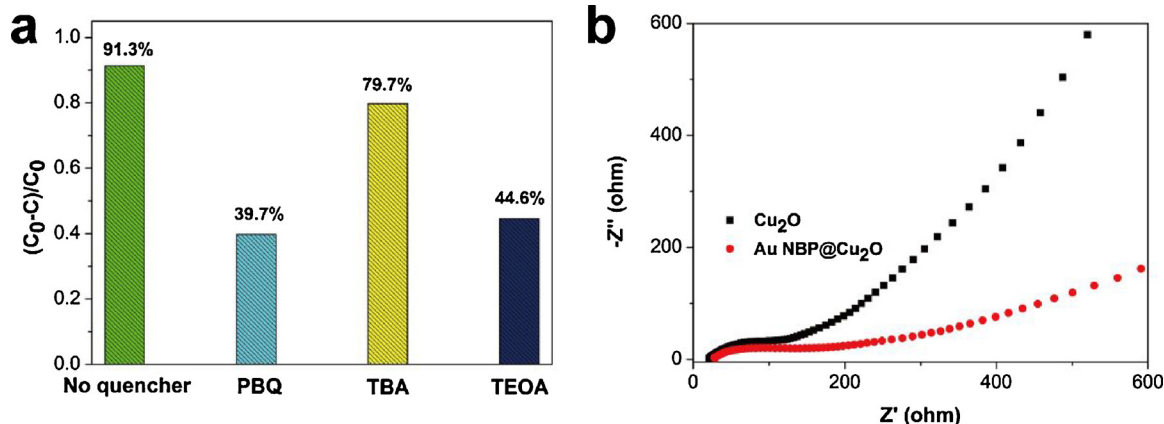

Fig. 10. (a) Reactive species trapping experiment for Au NBP@Cu$_2$O composites in the photodegradation of MO under illumination (λ > 400 nm). (b) EIS measurements for pure Cu$_2$O and Au NBP@Cu$_2$O composites, respectively.

the stellated structure are also important to the improved photo-catalytic performance of Au NBP@Cu$_2$O. We believe our work would provide a guide for the fabrication of Au NBPs and Cu$_2$O or other semiconductor composites and the exploration of applications for them, such as near-infrared-light-driven photocatalysis.

Acknowledgements

Appendix A. Supplementary data

Supplementary material related to this article can be found, in the online version, at doi:https://doi.org/10.1016/j.apcatb.2018.04.014.

References

[1] A. Ibhadon, P. Fitzpatrick, Catalysts 3 (2013) 189–218.
[2] H. Gao, J. Zhang, R. Wang, M. Wang, Appl. Catal.. B: Environ. (172–173) (2015) 1–6.
[3] J.B. Joo, R. Dillon, I. Lee, Y. Yin, C.J. Bardeen, F. Zaera, Proc. Natl. Acad. Sci. U. S. A. 111 (2014) 7942–7947.
[4] K. Mondal, A. Sharma, RSC Adv. 6 (2016) 83589–83612.
[5] T. Hisatomi, J. Kubota, K. Domen, Chem. Soc. Rev. 43 (2014) 7520–7535.
[6] H. Wang, L. Zhang, Z. Chen, J. Hu, S. Li, Z. Wang, J. Liu, X. Wang, Chem. Soc. Rev. 43 (2014) 5234–5244.
[7] R. Marschall, Adv. Funct. Mater. 24 (2014) 2421–2440.
[8] K.M. Lee, C.W. Lai, K.S. Ngai, J.C. Juan, Water Res. 88 (2016) 428–448.
[9] G.F. Samu, Ágnes Veres, S.P. Tallósy, L. Janovák, I. Dékány, A. Yepez, R. Luque, C. Janáky, Catal. Today 284 (2017) 3–10.
[10] S. Li, J. Cai, X. Wu, F. Zheng, X. Lin, W. Liang, J. Chen, J. Zheng, Z. Lai, T. Chen, L. Zhu, Appl. Catal. B: Environ. (160–161) (2014) 279–285.
[11] M. Ebrahimi, M. Samadi, S. Yousefzadeh, M. Soltani, A. Rahimi, T.C. Chou, L.C. Chen, K.H. Chen, A.Z. Moshfegh, A.C.S. Sustain. Chem. Eng. 5 (2016) 367–375.
[12] Y. Yan, Q. Liu, X. Du, J. Qian, H. Mao, K. Wang, Anal. Chim. Acta. 853 (2015) 258–264.
[13] Y. Xu, H. Wang, Y. Yu, L. Tian, W. Zhao, B. Zhang, J. Phys. Chem. C 115 (2011) 15288–15296.
[14] W. Huang, L. Lyu, Y. Yang, M.H. Huang, J. Am. Chem. Soc. 134 (2012) 1261–1267.
[15] J. Chen, S. Shen, P. Guo, M. Wang, P. Wu, X. Wang, L. Guo, Appl. Catal. B: Environ. (152–153) (2014) 335–341.
[16] T. Aditya, J. Jana, N.K. Singh, A. Pal, T. Pal, ACS Omega 2 (2017) 1968–1984.
[17] L. Zhang, D. Jing, L. Guo, X. Yao, A.C.S. Sustain. Chem. Eng. 2 (2014) 1446–1452.
[18] X. Han, X. He, F. Wang, J. Chen, J. Xu, X. Wang, X. Han, J. Mater. Chem. A 5 (2017) 10220–10226.
[19] Q. Zhai, S. Xie, W. Fan, Q. Zhang, Y. Wang, W. Deng, Y. Wang, Angew. Chemie. Int. Ed. 52 (2013) 5776–5779.
[20] J. Li, S.K. Cushing, J. Bright, F. Meng, T.R. Senty, P. Zheng, A.D. Bristow, N. Wu, J.T. Li, S.K. Cushing, J. Bright, F. Meng, T.R. Senty, P. Zheng, A.D. Bristow, N.Q. Wu, ACS Catal. 3 (2013) 47–51.
[21] J. Zhao, T. Zheng, J. Gao, S. Guo, X. Zhou, W. Xu, Analyst 142 (2017) 794–799.
[22] P.D. Tran, S.K. Batabyal, S.S. Pramana, J. Barber, L.H. Wong, S.C.J. Loo, Nanoscale 4 (2012) 3875–3878.
[23] X. An, K. Li, J. Tang, ChemSusChem. 7 (2014) 1086–1093.
[24] H. Li, X. Zhang, D.R. MacFarlane, Adv. Energy Mater. 5 (2015) 1401077.
[25] S.C. Wu, C.S. Tan, M.H. Huang, Adv. Funct. Mater. 1604635 (2017) 1604635.
[26] D. Jiang, W. Zhou, X. Zhong, Y. Zhang, X. Li, ACS Appl. Mater. Interfaces 6 (2014) 10958–10962.
[27] L. Kong, W. Chen, D. Ma, Y. Yang, S.S. Liu, S.M. Huang, J. Mater. Chem. 22 (2012) 719–724.
[28] Z. Yang, Z. Li, X. Lu, F. He, X. Zhu, Y. Ma, R. He, F. Gao, W. Ni, Y. Yi, Nano–Micro Lett. 9 (2017) 138–146.
[29] X. Wu, J. Cai, S. Li, F. Zheng, Z. Lai, L. Zhu, T. Chen, J. Colloid Interface Sci. 469 (2016) 138–146.
[30] Q. Ruan, L. Shao, Y. Shu, J. Wang, H. Wu, Adv. Opt. Mater. 2 (2014) 65–73.
[31] Z. Yang, Z.H. Li, X.X. Lu, F.J. He, X.Z. Zhu, Y.J. Ma, R. He, F. Gao, W.H. Ni, Y.S. Yi, Nano-Micro Lett. 9 (2017) 5.
[32] M. Chirea, A. Freitas, B.S. Vasile, C. Ghitulica, C.M. Pereira, F. Silva, Langmuir 27 (2011) 3906–3913.
[33] H. Yao, D. Mo, J. Duan, Y. Chen, J. Liu, Y. Sun, M. Hou, T. Schäpers, Appl. Surf. Sci. 258 (2011) 147–150.
[34] T. Ming, W. Feng, Q. Tang, F. Wang, L. Sun, J. Wang, C.H. Yan, J. Am. Chem. Soc. 131 (2009) 16350–16351.
[35] X.S. Kou, Z.H. Sun, Z. Yang, H.J. Chen, J.F. Wang, Langmuir 25 (2009) 1692–1698.
[36] X. Kou, S. Zhang, C. Tsung, M.H. Yeung, Q. Shi, G.D. Stucky, L. Sun, J. Wang, C. Yan, J. Phys. Chem. B 110 (2006) 16377–16383.
[37] W. Ni, X. Kou, Z. Yang, J. Wang, ACS Nano 2 (2008) 677–686.
[38] L. Vigderman, E.R. Zubarev, Chem. Mater. 25 (2013) 1450–1457.
[39] X. Kou, W. Ni, C. Tsung, K. Chan, H. Lin, G.D. Stucky, J. Wang, Small 3 (2007) 2103–2113.
[40] (a) Q. Li, X. Zhuo, S. Li, Q. Ruan, Q.H. Xu, J.F. Wang, Adv. Opt. Mater. 3 (2015) 801–812;
(b) X.L. Zhuo, X.Z. Zhu, Q. Li, Z. Yang, J.F. Wang, ACS Nano 9 (2015) 7523–7535.
[41] A. Li, P. Zhang, X. Chang, W. Cai, T. Wang, J. Gong, Small 16 (2015) 1892–1899.
[42] X.Z. Zhu, X. Zhuo, Q. Li, Z. Yang, J.F. Wang, Adv. Funct. Mater. 26 (2016) 341–352.
[43] X. Yu, F. Liu, J. Bi, B. Wang, S. Yang, Nano Energy 33 (2017) 469–475.
[44] Y. Pan, S. Deng, L. Polavarapu, N. Gao, P. Yuan, C.H. Sow, Q. Xu, Langmuir 28 (2012) 12304–12310.
[45] J. Niu, Y. Dai, L. Yin, J. Shang, J.C. Crittenden, Phys. Chem. Chem. Phys. 17 (2015) 17421–17428.
[46] G.Z. Yuan, C.F. Hsia, Z.W. Lin, C. Chiang, Y.W. Chiang, M.H. Huang, Chem. Eur. J. 22 (2016) 12548–12556.
[47] C. Fang, H. Jia, S. Chang, Q. Ruan, P. Wang, T. Chen, J. Wang, Energy Environ. Sci. 7 (2014) 3431–3438.
[48] B. Lu, A. Liu, H. Wu, Q. Shen, T. Zhao, J. Wang, Langmuir 32 (2016) 3085–3094.
[49] L. Zhang, D.A. Blom, H. Wang, Chem. Mater. 23 (2011) 4587–4598.
[50] Y.C. Yang, H.J. Wang, J. Whang, J.S. Huang, L.M. Lyu, P.H. Lin, S. Gwo, M.H. Huang, Nanoscale 6 (2014) 4316–4324.
[51] H. Wang, K. Yang, S. Hsu, M.H. Huang, Nanoscale 8 (2016) 965–972.
[52] Q. Yuan, L. Chen, M. Xiong, J. He, S.L. Luo, C.T. Au, S.F. Yin, Chem. Eng. J. 255 (2014) 394–402.
[53] X. Shi, Y. Ji, S. Hou, W. Liu, H. Zhang, T. Wen, J. Yan, M. Song, Z. Hu, X. Wu, X.W. Shi, Y.L. Ji, S. Hou, W.Q. Liu, H. Zhang, T. Wen, J. Yan, Z. Min Song, J. Hu, X.C. Wu, Nanoscale 8 (2016) 965–972.
[54] S. Hsu, S.Y. Liu, H.J. Wang, M.H. Huang, Small 11 (2015) 195–201.
[55] C.H. Kuo, Y.C. Yang, S.J. Gwo, M.H. Huang, J. Am. Chem. Soc. 133 (2011) 1052–1057.
[56] C.S. Tan, S.C. Hsu, W.H. Ke, L.J. Chen, M.H. Huang, Nano Lett. 15 (2015) 2155–2160.
[57] G.Z. Yuan, C.F. Hsia, Z.W. Lin, C. Chiang, Y.W. Chiang, M.H. Huang, Chem. Eur. J. 22 (2016) 12548–12556.
[58] H.J. Wang, K.H. Yang, S.C. Hsu, M.H. Huang, Nanoscale 8 (2016) 965–972.
[59] N.E. Singh-Miller, N. Marzari, Phys. Rev. B 80 (2009) 235407.
[60] H.L. Zhuang, A.J. Tkalych, E.A. Carter, J. Phys. Chem. C 120 (2016) 23698–23706.
[61] L.L. Wang, J. Ge, A. Wang, M.S. Deng, X.J. Wang, S. Bai, R. Li, J. Jiang, Q. Zhang, Y. Luo, Y.J. Xiong, Angew. Chem. 126 (2014) 5207–5211.
[62] S. Bai, J. Ge, L.L. Wang, M. Gong, M.S. Deng, Q. Kong, L. Song, J. Jiang, Q. Zhang, Y. Luo, Y. Xie, Y.J. Xiong, Adv. Mater. 26 (2014) 5689–5695.
[63] Z.K. Zheng, B.B. Huang, Z.Y. Wang, M. Guo, X.Y. Qin, X.Y. Zhang, P. Wang, Y. Dai, J. Phys. Chem. C 113 (2009) 14448–14453.
[64] Q. Li, X. Li, S. Wageh, A.A. Al-Ghamdi, J.G. Yu, Adv. Energy Mater. 5 (2015) 1500010.
[65] K.F. Wu, W.E. Rodríguez-Córdoba, Y. Yang, T.Q. Lian, Nano Lett. 13 (2013) 5255–5263.
[66] J. Cai, X. Wu, S. Li, F. Zheng, L. Zhu, Z. Lai, ACS Appl. Mater. Interfaces 7 (2015) 3764–3772.
[67] J. Wang, Y. Li, J. Ge, B. Zhang, W. Wan, Phys. Chem. Chem. Phys. 17 (2015) 18645–18652.